International Journal of Bifurcation and Chaos, Vol. 13, No. 5 (2003) 1275–1286

STREAMLINE TOPOLOGY AND DILUTE PARTICLE DYNAMICS IN A KÁRMÁN VORTEX STREET FLOW

ZUO-BING WU
State Key Laboratory of Nonlinear Mechanics,
Institute of Mechanics, Academia Sinica, Beijing 100080, China
wuzb@lnm.imech.ac.cn

Received January 29, 2002; Revised March 23, 2002

Three types of streamline topology in a Kármán vortex street flow are shown under the variation of spatial parameters. For the motion of dilute particles in the Kármán vortex street flow, there exist a route of bifurcation to a chaotic orbit and more attractors in a bifurcation diagram for the proportion of particle density to fluid density. Along with the increase of spatial parameters in the flow field, the bifurcation process is suspended, as well as more and more attractors emerge. In the motion of dilute particles, a drag term and gravity term dominate and result in the bifurcation phenomenon.

Keywords: Topological flow field; dilute particle dynamics; bifurcation to chaos.

1. Introduction

The motions of particles in a nonuniform flow have wide technological applications, such as to forecast chemical reactions and environmental pollution. Due to particle motion in the low Reynolds number category, the equation of motion for a small rigid sphere in a nonuniform flow field is deduced [Maxey & Riley, 1983]. When the background flow is mainly dominated by large scale structures, the fluid viscosity is not included in the governing flow equation [Chung & Troutt, 1988]. Related studies show that even when the background flow fields are very simple, the motions can have abundant phenomena. In a periodic Stuart vortex flow, depending on the values of parameters, the particles asymptotically concentrate along periodic, quasiperiodic or chaotic open trajectory [Ganan-Calvo & Lasheras, 1991; Tio *et al.*, 1993]. In a cellular flow field, aerosol particles also merge into isolated asymptotic trajectories, which are described by slow manifolds [Maxey, 1997; Rubin *et al.*, 1995]. Moreover, the method due to the Lagrange view of particles can also be applied to investigate effects of particle dispersion on streamwise braid vortices in a plane mixing layer [Marcu & Meiburg, 1996; Marcu *et al.*, 1996].

In a plane wake flow behind a circular cylinder, a regular vortex street structure was investigated at $\mathrm{Re} = 60 - 5000$. Along with the advance of experimental techniques, even at $\mathrm{Re} = O(10^4)$, the regular vortex street is obtained by using the phase-average method [Hussain & Hayakawa, 1987]. In particular, the phenomena relating to organized vortex structure, such as, reconnection of vortex street [Okude, 1981] and emergence of three-dimensional vortex structure [Willimson, 1988], arouse wide interest for the transition of a plane wake flow. Recently, particle focusing in narrow bands near the peripheries of the vortex structures for the particle dispersion in a plane wake flow is observed experimentally [Tang *et al.*, 1992]. By considering Stokes drag, the phenomenon of particle focusing is studied on two-dimensional centre manifolds [Burns *et al.*, 1999]. The regular Kármán vortex street flow as a model to approach the plane wake flow and investigate the above phenomena plays an important role.

For the motion of particles in regular vortex street flow, Kármán vortex spacing influences the

topological structure of background flow field. At the same time, a density ratio as a basic parameter may have a wide range. In this paper, we will consider streamline topology and dilute particle dynamics in the Kármán vortex street flow in a range of density ratio. In Sec. 2, it is shown that for the Kármán vortex street flow, there exist three types of global topological structure depending on the spatial parameters in flow field. Dilute particle dynamics in the Kármán vortex street flow related to the density ratio is investigated in Sec. 3. Effects of spatial parameters in flow field on dilute particle dispersion are determined in Sec. 4. Finally, a brief summary is given in Sec. 5.

2. Streamline Topology

The stream function of Kármán vortex street flow [Milne-Thomson, 1979] is

$$\Psi(x,\,y)=\frac{\Gamma}{4\pi}\,\ln\frac{\operatorname{ch}\dfrac{2\pi}{l}\,(y-h/2)-\cos\dfrac{2\pi}{l}\,x}{\operatorname{ch}\dfrac{2\pi}{l}(y+h/2)+\cos\dfrac{2\pi}{l}\,x}+\frac{\Gamma y}{2l}\operatorname{th}\frac{\pi h}{l}\,, \tag{1}$$

where Γ is the strength of vortices, l and h are the streamwise and transverse spacing of vortices, respectively. The dimensionless quantities denoted by asterisks are introduced as $x^*=x/l$, $y^*=y/l$, $h^*=h/l$, $u^*=u/U_\infty$, $\Gamma^*=\Gamma/(U_\infty l)$ and $\Psi^*=\Psi/(U_\infty l)$. The stream function (1) can be represented as

$$\Psi^*(x^*,\,y^*)=\frac{\Gamma^*}{4\pi}\,\ln\frac{\operatorname{ch}2\pi(y^*-h^*/2)-\cos\,2\pi x^*}{\operatorname{ch}2\pi(y^*+h^*/2)+\cos\,2\pi x^*}+\frac{\Gamma^* y^*}{2}\operatorname{th}\pi h^*\,. \tag{2}$$

From now on, the asterisks "*" for the dimensionless quantities in this section are omitted for convenience. The stream function (2) has symmetries: $\Psi(x+1/2,\,-y)=-\Psi(x,\,y)$, $\Psi(x+1,\,y)=\Psi(x,\,y)$.

The associated velocity field is given by

$$\begin{aligned}
u_x&=\frac{\partial\Psi}{\partial y}=\frac{\Gamma}{2}\left[\frac{\operatorname{sh}2\pi(y-h/2)}{\operatorname{ch}2\pi(y-h/2)-\cos\,2\pi x}-\frac{\operatorname{sh}2\pi(y+h/2)}{\operatorname{ch}2\pi(y+h/2)+\cos\,2\pi x}\right]+\frac{\Gamma}{2}\operatorname{th}\pi h\,,\\
u_y&=-\frac{\partial\Psi}{\partial x}=-\frac{\Gamma}{2}\left[\frac{1}{\operatorname{ch}2\pi(y-h/2)-\cos\,2\pi x}+\frac{1}{\operatorname{ch}2\pi(y+h/2)+\cos\,2\pi x}\right]\sin\,2\pi x\,,
\end{aligned} \tag{3}$$

which has singularity at the vortex centers. In the case of removing the singularity by the Rankine vortex [Wu & Ling, 1994], free stagnation points in velocity field (3) consist of centers and saddle points, which can be respectively described by $(0,\,h/2)$, $(1/2,\,-(h/2))$ and $(0,\,-(1/2\pi)\ln c,\ (1/2,\,(1/2\pi)\ln c)$, where $c=2/\operatorname{sh}\pi h+\operatorname{sh}\pi h+\sqrt{[2/\operatorname{sh}\pi h+\operatorname{sh}\pi h]^2+1}$.

In the symmetry $\Psi(x+1/2,\,-y)=-\Psi(x,\,y)$, it can be shown that there exists a zero streamline between two neighboring centers $(0,\,h/2)$ and $(1/2,\,-(h/2))$. Under the variation of spatial parameter h, we take zero streamlines to investigate the evolution of global topological structure. The points y_0, corresponding to zero streamlines passing through the y coordinate, satisfy

$$\begin{aligned}
\Psi(0,\,y_0)&=\frac{\Gamma}{4\pi}\,\ln\frac{\operatorname{ch}2\pi(y_0-h/2)-1}{\operatorname{ch}2\pi(y_0+h/2)+1}+\frac{\Gamma y_0}{2}\operatorname{th}\pi h\\
&=0\,.
\end{aligned} \tag{4}$$

Using the Newton–Raphson and bisection methods [Press *et al.*, 1992], we solve Eq. (4) and plot the relation $y_0\sim h$ in Fig. 1.

When $h=0$, the Kármán vortex street returns to a periodic row of vortex pair ($u_x=$

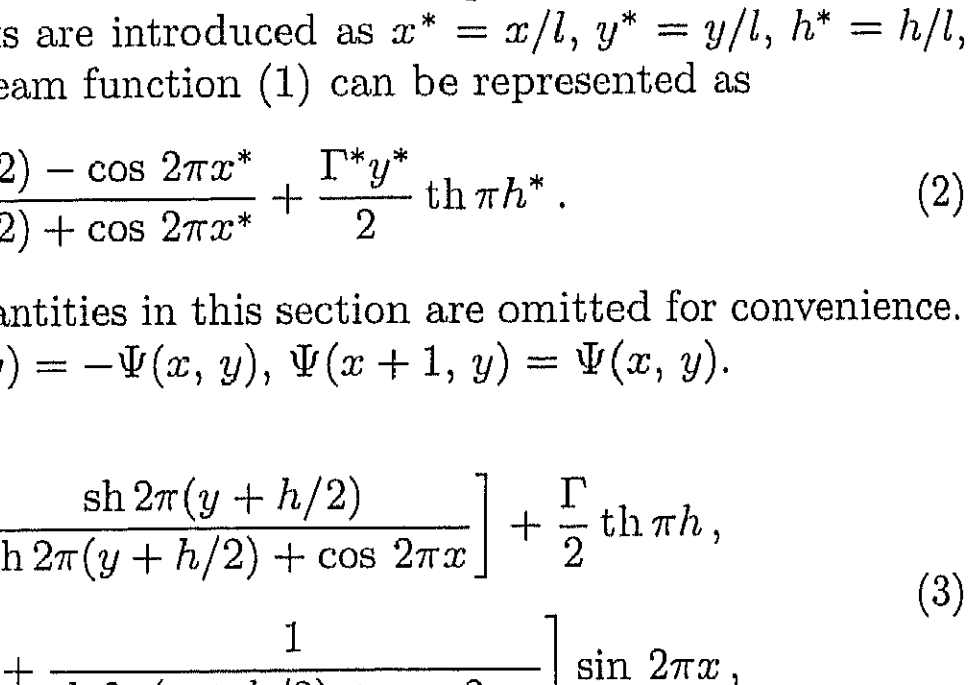

Fig. 1. Points of zero streamlines in the y coordinate.

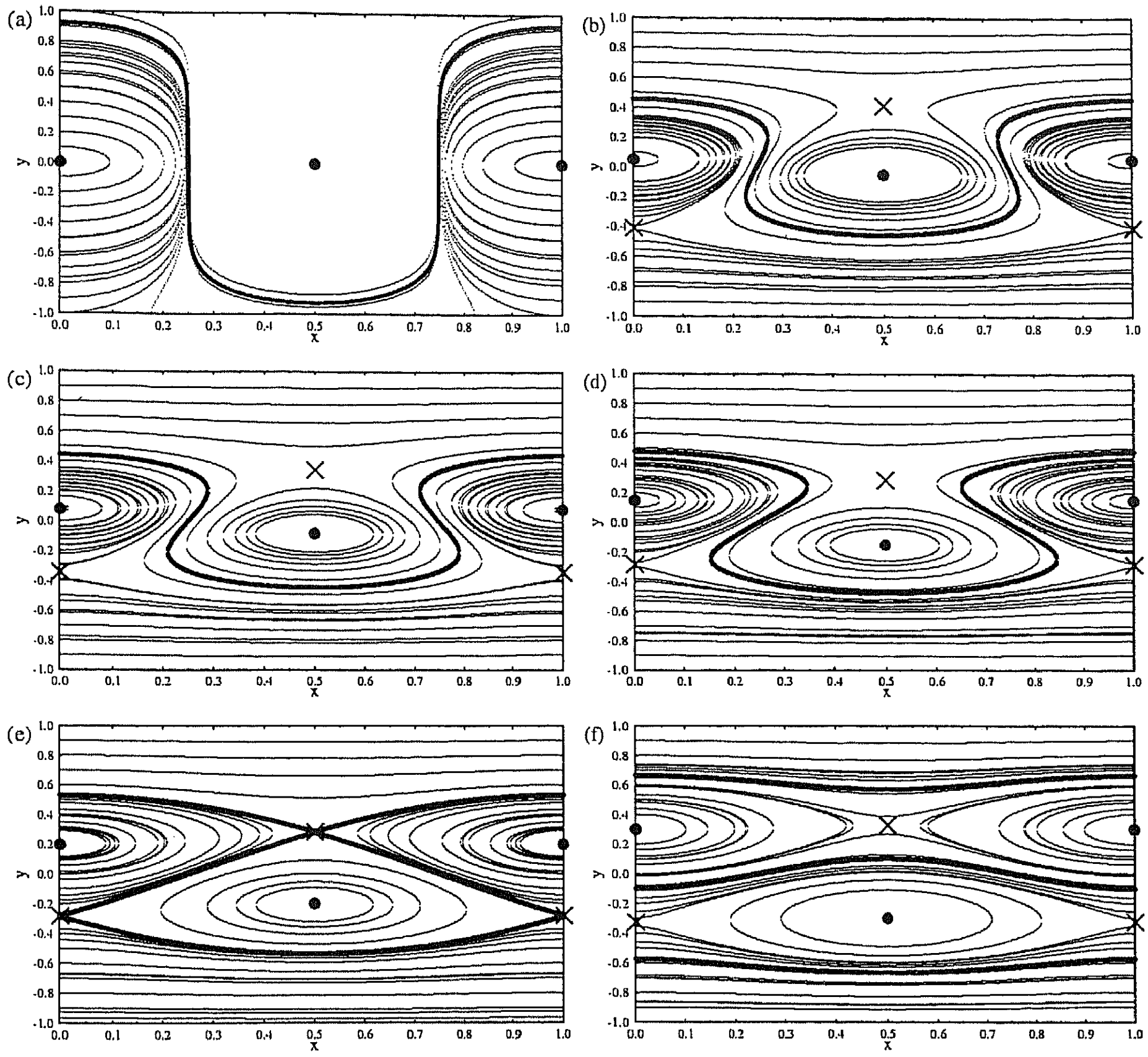

Fig. 2. All streamlines including corresponding embedded zero streamlines with centers marked by dots and saddle points marked by crosses for (a) $h = 0.001$; (b) $h = 0.1$; (c) $h = 0.164$; (d) $h = 0.3$; (e) $h = 0.410998$; (f) $h = 0.6$.

$\Gamma \cos 2\pi x \,\mathrm{sh}\, 2\pi y/(\mathrm{ch}^2 2\pi y - \cos^2 2\pi x)$ and $u_y = -\Gamma \sin 2\pi x \,\mathrm{ch}\, 2\pi y/(\mathrm{ch}^2 2\pi y - \cos^2 2\pi x)$). In this case, a zero streamline exists in $y_0 = \infty$, as well as free stagnation points are only centers. All streamlines including an embedded zero streamline for $h = 0.001$, which approach to those for $h = 0$, are drawn in Fig. 2(a). Two neighboring vortices are divided by the zero streamline. In Fig. 1, there exists a minimum point (0.164, 0.443434) marked by o. To understand this point, we take the derivative of $\Psi(0, y)$ with respect to h, as follows,

$$\frac{\partial \Psi(0, y)}{\partial h} = -\frac{\Gamma}{4}\left[\frac{\mathrm{sh}\, 2\pi(y - h/2)}{\mathrm{ch}\, 2\pi(y - h/2) - 1} + \frac{\mathrm{sh}\, 2\pi(y + h/2)}{\mathrm{ch}\, 2\pi(y + h/2) + 1} - \frac{2\pi y}{\mathrm{ch}^2 \pi h}\right] = 0\,. \tag{5}$$

Using the Newton–Raphson and bisection methods [Press *et al.*, 1992], we solve Eq. (5) and plot the solutions in Fig. 3(a). Besides a trivial solution $y = h/2$ of Eq. (5), other relations $\pm y \sim h$ are symmetrical and corresponding to the maximum and minimum of $\Psi(0, y)$ for h. The point (0.164, 0.443434) exists in the curve $y \sim h$ marked

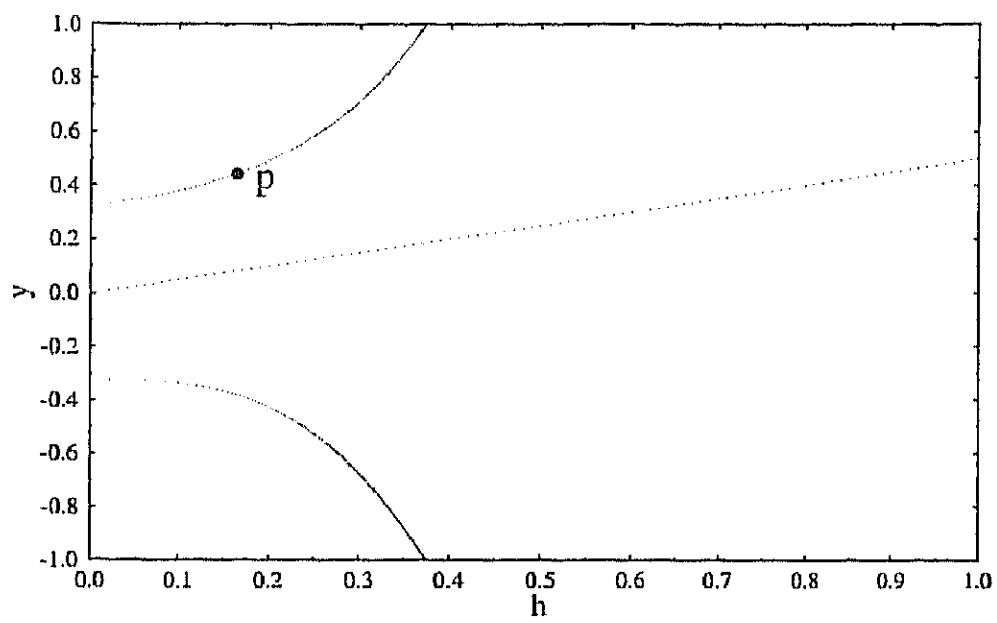

(a)

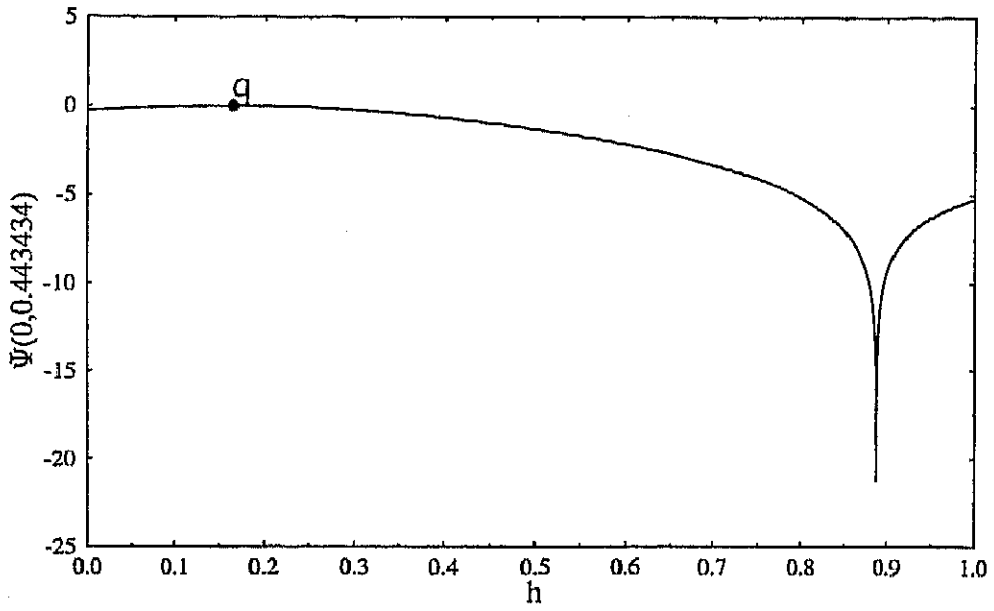

(b)

Fig. 3. (a) A relation $y \sim h$ for $\Psi_{\max/\min}(0, y)$; (b) Stream function relating to h at $(0, 0.443434)$.

by p, so that $\Psi(0, 0.443434)$ is a maximum of $\Psi(0, y)$ for h. We also plot the relation of $\Psi(0, 0.443434)$ to h in Fig. 3(b). The maximum point q in the curve confirms to the above result. Thus, the minimum point in Fig. 1 corresponds to the maximum of $\Psi(0, y)$ for h.

When h increases from 0 to 0.164, y_0 monotonically decreases from ∞ to 0.443434 in Fig. 1. All streamlines including an embedded zero streamline for $h = 0.1$ are drawn in Fig. 2(b). In this case, saddle points emerge below or above the centers in opposition to the zero streamlines. The orbits passing through saddle points go around the centers and come back, as well as go to other saddle points, i.e. there exist homoclinic and heteroclinic orbits. For $h = 0.164$, all streamlines including an embedded zero streamline are drawn in Fig. 2(c). When h increases from 0.164, y_0 monotonically increases from 0.443434 in Fig. 1. All streamlines including an embedded zero streamline for $h = 0.3$ are drawn in Fig. 2(d). When h increases to 0.410998, another solution of y_0 emerges in Fig. 1. All associated streamlines including embedded zero streamlines are drawn in Fig. 2(e). Zero streamlines, surrounding each vortex, pass through the saddle points. So, the zero streamlines are homoclinic and heteroclinic orbits. When h increases beyond 0.410998, the solution becomes two ones in Fig. 1. At the time, there exist three zero streamlines. The orbits passing through saddle points go around the centers and to other saddle points, but do not come back, i.e. there exist only heteroclinic orbits. All streamlines including three embedded zero streamlines for $h = 0.6$ are drawn in Fig. 2(f). Upper and lower vortices are divided by one zero streamline, as well as surrounded by others.

In the experiment of a plane wake flow [Okude & Matsui, 1987], it has been shown that h increases downstream from 0.2 to 0.45 at $\mathrm{Re} = 140$. We can thus conclude that three types of streamline topology can emerge in a plane wake flow.

3. Dilute Particle Dynamics

3.1. *Governing equations*

The motion of a small spherical particle in a nonuniform flow field $\mathbf{u}$ is governed by the momentum equation [Maxey & Riley, 1983; Tio *et al.*, 1993]

$$\begin{aligned}
&\frac{\pi}{6} d^3(\rho_P + 0.5\rho_F) \frac{d\mathbf{V}}{dt} \\
&\quad = \frac{\pi}{6} d^3(\rho_P - \rho_F)\mathbf{g} \\
&\qquad + \frac{\pi}{4} d^3 \rho_F \frac{D\mathbf{u}}{Dt} + 3\pi d\nu\rho_F(\mathbf{u} - \mathbf{V}) f_d \\
&\qquad + \frac{3}{2}(\pi\nu)^{1/2} d^2 \rho_F \int_0^t \frac{1}{\sqrt{t-\tau}} \left(\frac{d\mathbf{u}}{d\tau} - \frac{d\mathbf{V}}{d\tau}\right) d\tau \\
&\qquad + \frac{\pi}{12} d^3 \rho_F (\mathbf{u} - \mathbf{V}) \times \omega \,, \qquad (6)
\end{aligned}$$

where $\mathbf{V}$ is the velocity of the particle, d is the particle diameter, ρ is the density, $\mathbf{g}$ is the gravitational acceleration, ν is the fluid kinematic viscosity, ω is the vorticity of the flow fluid, and the subscripts F and P refer to the fluid and particle, respectively. The parameter f_d relating to Reynolds number ($\mathrm{Re}_P = |\mathbf{u} - \mathbf{V}|d/\nu$) is described [Clift *et al.*, 1978; Tio *et al.*, 1993] as

$$f_d = 1 + 0.1315\,\mathrm{Re}_P^{0.82 - 0.05\log_{10}\mathrm{Re}_P}\,,$$
$$0 < \mathrm{Re}_P < 200\,. \qquad (7)$$

Introducing the dimensionless quantities $\delta = \rho_P/\rho_F$, $\varepsilon = 1/(0.5+\delta)$, $t^* = t/T$, $\mathbf{V}^* = \mathbf{V}/(l/T)$ and $\mathbf{g}^* = \mathbf{g}/g$ (T is the particle viscous relaxation time $d^2/(18\varepsilon\nu)$), we nondimensionlize Eq. (6) and ignore the Basset history term. Thus, Eq. (6) can be described by

$$\frac{d\mathbf{V}}{dt} = B\mathbf{g} + \frac{3}{2}\varepsilon A^2\mathbf{u}\bullet\nabla\mathbf{u} + (A\mathbf{u}-\mathbf{V})f_d + \frac{1}{2}\varepsilon A(A\mathbf{u}-\mathbf{V})\times\omega\,, \tag{8}$$

where $A = U_\infty T/l$, $B = (1-1.5\varepsilon)T^2(g/l)$ and the asterisks "*" for the dimensionless quantities in this section are omitted for convenience. Moreover, the Reynolds number is written as $\mathrm{Re}_P = \overline{\mathrm{Re}}_P/A|A\mathbf{u}-\mathbf{V}|$ ($\overline{\mathrm{Re}}_P = U_\infty d/\nu$).

The flow field $\mathbf{u}$ is chosen to be the Kármán vortex street flow (3), where a parameter k is introduced to remove the singularities. The modified stream function (2) is described as

$$\Psi(x,y) = \frac{\Gamma}{4\pi}\ln\frac{\mathrm{ch}\,2\pi(y-h/2)-k\cos 2\pi x}{\mathrm{ch}\,2\pi(y+h/2)+k\cos 2\pi x} + \frac{\Gamma y}{2}\frac{\mathrm{sh}\,2\pi h}{\mathrm{ch}\,2\pi h+k}. \tag{9}$$

The corresponding velocity field is given by

$$\begin{aligned} u_x &= \frac{\partial\Psi}{\partial y} = \frac{\Gamma}{2}\left[\frac{\mathrm{sh}\,2\pi(y-h/2)}{\mathrm{ch}\,2\pi(y-h/2)-k\cos 2\pi x} - \frac{\mathrm{sh}\,2\pi(y+h/2)}{\mathrm{ch}\,2\pi(y+h/2)+k\cos 2\pi x}\right] + \frac{\Gamma}{2}\frac{\mathrm{sh}\,2\pi h}{\mathrm{ch}\,2\pi h+k}\,,\\ u_y &= -\frac{\partial\Psi}{\partial x} = -\frac{\Gamma k}{2}\left[\frac{1}{\mathrm{ch}\,2\pi(y-h/2)-k\cos 2\pi x} + \frac{1}{\mathrm{ch}\,2\pi(y+h/2)+k\cos 2\pi x}\right]\sin 2\pi x\,. \end{aligned} \tag{10}$$

Only when $k=1$, the velocity field satisfies the Euler equation. Since the error increases with deviation of k from 1, we take $k=0.99$ as an approximation in this simulation.

The particle motion is described by a four-dimensional, nonlinear autonomous dynamical system of the form

$$\begin{aligned} \dot{x} &= V_x\,,\\ \dot{y} &= V_y\,,\\ \dot{V}_x &= \frac{3}{2}\varepsilon A^2\mathbf{u}\bullet\nabla u_x + (Au_x - V_x)f_d + \frac{1}{2}\varepsilon A\omega(Au_y - V_y)\,,\\ \dot{V}_y &= \frac{3}{2}\varepsilon A^2\mathbf{u}\bullet\nabla u_y + (Au_y - V_y)f_d - \frac{1}{2}\varepsilon A\omega(Au_x - V_x) - B\,. \end{aligned} \tag{11}$$

The parameters in Eqs. (11) can be taken as $U_\infty = 4$ m/s and $d = 5\times10^{-5}$ m from [Tang *et al.*, 1992]. Since air is chosen as the fluid media in the flow, the properties of fluid in Eqs. (11) are described as $\rho = 1.225$ kg/m^3 and $\nu = 1.45\times10^{-5}$ m^2/s [Panton, 1984]. Moreover, the parameters concerning the Kármán vortex street flow are chosen as $l = 0.1$ m, $h = 0.3$ and $\Gamma = 1$. In the following, we investigate the motion of particles under the variation of density ratio δ. Initial values of particles are taken as points in the flow field and their corresponding flow field velocity. Using a fourth-order Runge–Kutta algorithm, we integrate Eqs. (11) with a time size $\tau = 0.001$. After discarding transients, we plot points at $x=0$ as a bifurcation diagram. When the time size is changed to $\tau = 0.01$, the bifurcation diagram is still preserved.

In order to understand the dilute particle dynamics, we analyze orders of magnitude of parameters in Eq. (8). For giving physical values in the calculation, the parameter f_d appear to be on the order 1. When δ is taken as the order $10^3 - 10^4$ and d is fixed as the order 10^{-5} m, the parameters ε, T, A and B appear to be on the order $10^{-3} - 10^{-4}$, 10^{-3} s $- 10^{-2}$ s, $10^{-2} - 10^{-1}$ and $10^{-4} - 10^{-2}$, respectively. In this case, the stress tensor term of fluid $(3/2)\varepsilon A^2\mathbf{u}\bullet\nabla\mathbf{u}$ and lift force term $(1/2)\varepsilon A(A\mathbf{u}-\mathbf{V})\times\omega$ have smaller orders than the drag term $(A\mathbf{u}-\mathbf{V})f_d$ and gravity term $B\mathbf{g}$ in Eq. (8). Therefore, Eq. (8) is dominated by the drag term and gravity term .

Moreover, concerning the stability of particle orbits, we take only the drag and gravity terms in Eq. (8) to obtain an approximate fundamental matrix $U^t_{\mathbf{x}}$. By using the straightforward technique [Shimada & Nagashima, 1979; Wolf *et al.*, 1985], a complete Lyapunov spectrum is determined

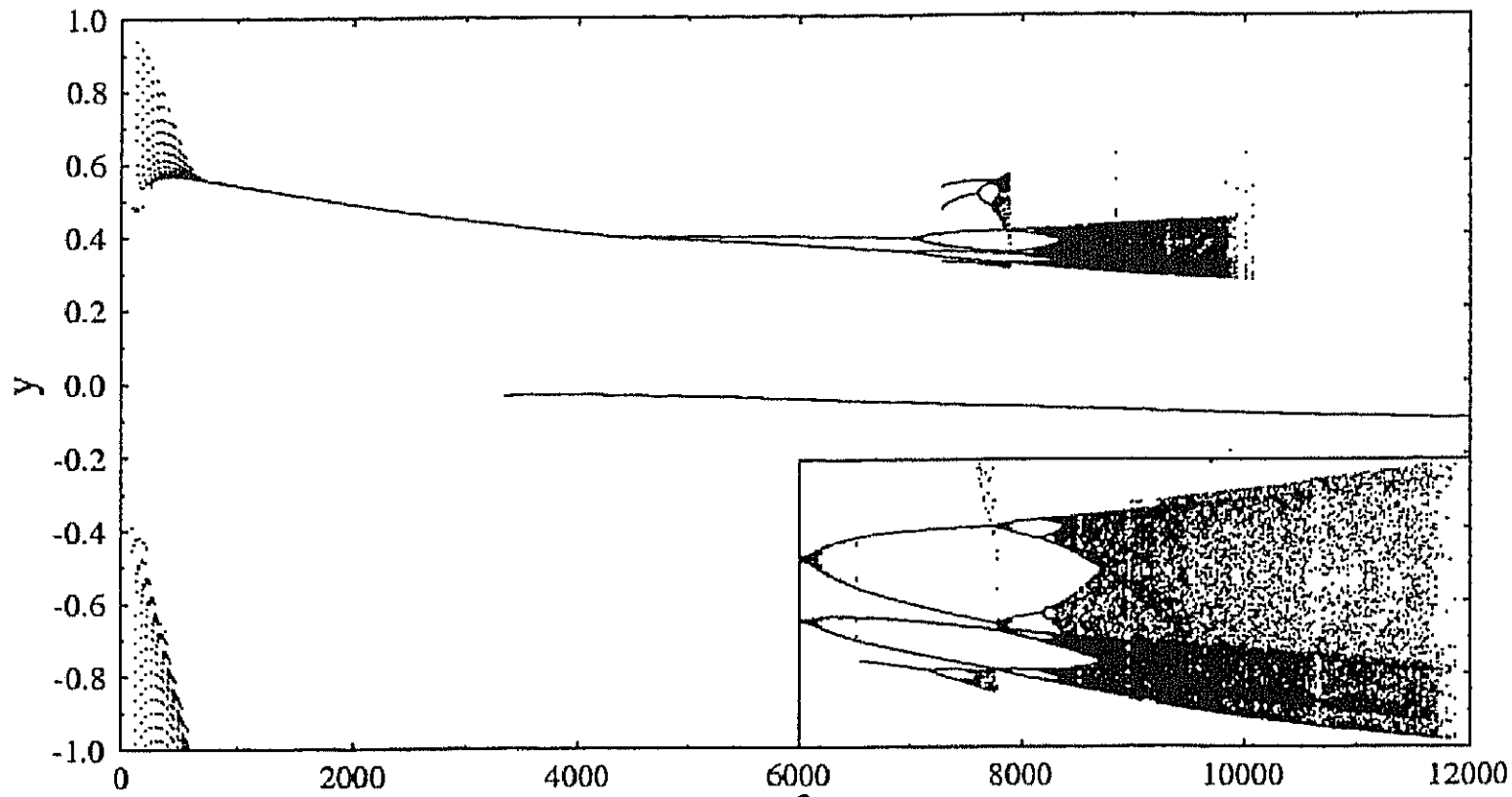

Fig. 4. A bifurcation diagram with $h = 0.3$ for a continuous range of δ showing the vertical position of particles at $x = 0$. The dense bifurcation zone $\delta \in [7000, 10000]$ above the street is enlarged and redrawn in the bottom-right corner of the figure.

as follows

$$\lambda = \lim_{t\to\infty} \frac{1}{t} \log \frac{\|U^t_{\mathbf{x}_0}\mathbf{e}^0_1 \wedge U^t_{\mathbf{x}_0}\mathbf{e}^0_2 \wedge U^t_{\mathbf{x}_0}\mathbf{e}^0_3 \wedge U^t_{\mathbf{x}_0}\mathbf{e}^0_4\|}{\|\mathbf{e}^0_1 \wedge \mathbf{e}^0_2 \wedge \mathbf{e}^0_3 \wedge \mathbf{e}^0_4\|}$$

$$= \lim_{n\to\infty} \frac{1}{n\tau} \Sigma_{i=0}^{n-1} \log \frac{\|U^\tau_{\mathbf{x}_i}\mathbf{e}^i_1 \wedge U^\tau_{\mathbf{x}_i}\mathbf{e}^i_2 \wedge U^\tau_{\mathbf{x}_i}\mathbf{e}^i_3 \wedge U^\tau_{\mathbf{x}_i}\mathbf{e}^i_4\|}{\|\mathbf{e}^i_1 \wedge \mathbf{e}^i_2 \wedge \mathbf{e}^i_3 \wedge \mathbf{e}^i_4\|}, \tag{12}$$

where $\wedge$ and $\|\circ\|$ are an exterior product and a norm with respect to the Riemannian metric, respectively. After each time integration, the set of bases $\{\mathbf{e}^i_1, \mathbf{e}^i_2, \mathbf{e}^i_3, \mathbf{e}^i_3\}$ is exchanged by using the Gram–Schmidt reorthonormalization procedure. In the calculation of the complete Lyapunov spectrum, the time size is taken as $\tau = 0.001$.

3.2. *Numerical results*

In Fig. 4, along with the increase of density ratio, a bifurcation diagram of y versus δ is drawn. When $\delta < 6.5 \times 10^2$, the velocity of particle dispersion is very slow, so most of the particle trajectories are preserved near the street. When $\delta \geq 6.5 \times 10^2$, besides the particle dispersion, global trajectories of particles converge to two attractors: one above the street, the other in the street. For the attractor above the street in $\delta = 6.5 \times 10^2 - 4.4 \times 10^3$, it evolves as a period-1 orbit. At $\delta = 4.4 \times 10^3$, the period-1 orbit bifurcates to a period-2 orbit. In $\delta = 4.4 \times 10^3 - 7.0 \times 10^3$, the attractor evolves as a period-2 orbit. At $\delta = 7.0 \times 10^3$, the period-2 orbit bifurcates to a period-4 orbit. In $\delta = 7.0 \times 10^3 - 7.9 \times 10^3$, the attractor evolves as a period-4 orbit. In $\delta = 7.9 \times 10^3 - 1.0 \times 10^4$, the period-4 orbit bifurcates to a period-8 orbit and further to a quasi-periodic or chaotic orbit. At $\delta = 1.0 \times 10^4$, a crisis happens, so that the quasi-periodic or chaotic orbit disappears. Moreover, at $\delta = 7.3 \times 10^3$, a period-3 orbit emerges as another attractor above the street. In $\delta = 7.3 \times 10^3 - 7.9 \times 10^3$, the period-3 orbit bifurcates further to a quasi-periodic or chaotic orbit. At $\delta = 7.9 \times 10^3$, a crisis happens, so that the quasi-periodic or chaotic orbit disappears. The bifurcation procedure of period-3 orbit differs from that for the three-dimensional Lorenz equation [Lorenz, 1963]. For the attractor in the street, a period-1 orbit emerges at $\delta = 3.3 \times 10^3$. It preserves in $\delta = 3.3 \times 10^3 - 1.2 \times 10^4$.

In Fig. 5, we plot some typical examples for different values of δ. A period-1 orbit above the street for $\delta = 1.0 \times 10^3$, as well as all corresponding streamlines are drawn in Fig. 5(a). On the period-1 orbit, the particles move from left to right. In Fig. 6, for the period-1 orbit, the maximal Lyapunov exponent is -0.230, so the orbit is stable. In order to display the dispersion of particles in the flow field, we also plot the basin of attraction in Fig. 7(a). In the motion of particles, the points corresponding to those in the basin of attraction suspend on the period-1 orbit. At the same time, the points corresponding to those outside the basin of attraction escape

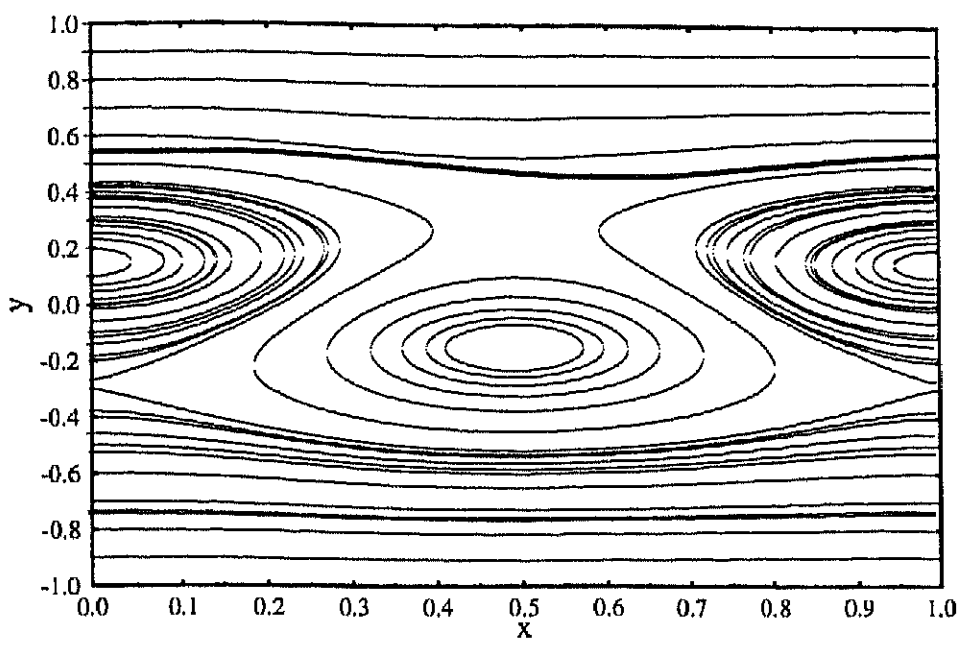

(a)

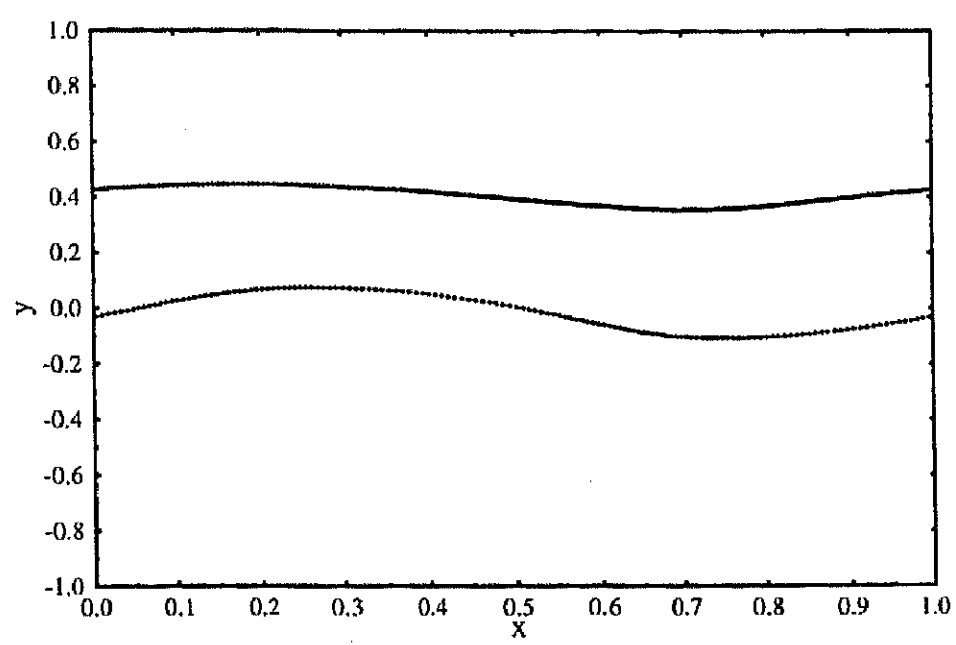

(b)

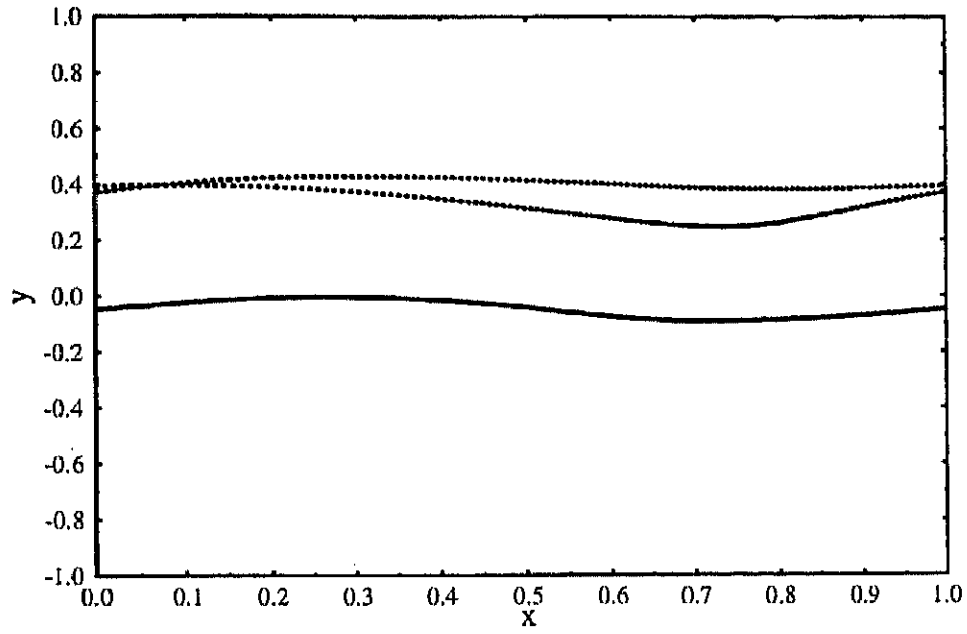

(c)

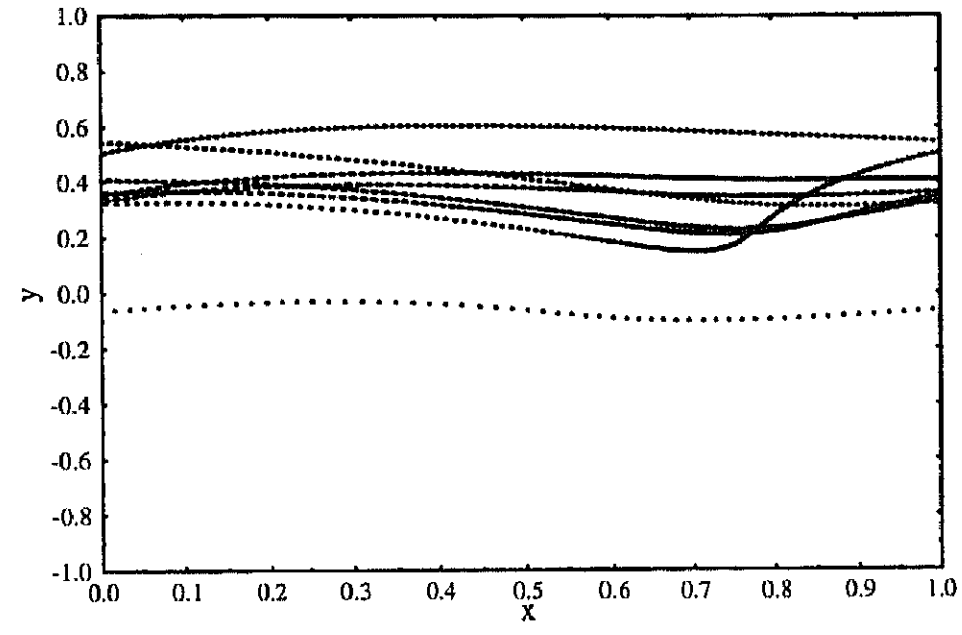

(d)

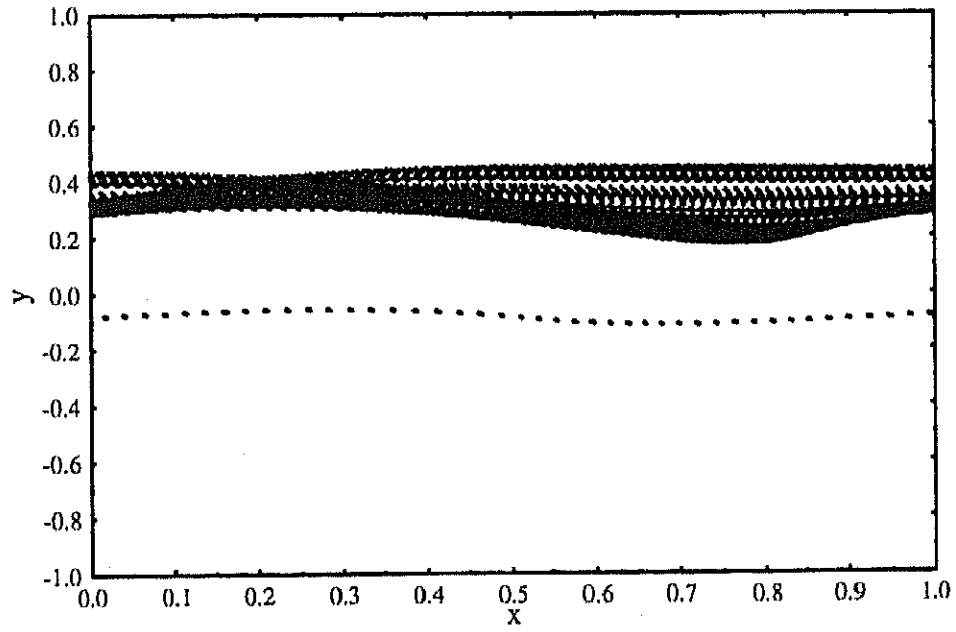

(e)

Fig. 5. Typical trajectories in Fig. 4 for (a) $\delta = 1.0 \times 10^3$ and all streamlines; (b) $\delta = 3.5 \times 10^3$; (c) $\delta = 6.0 \times 10^3$; (d) $\delta = 7.5 \times 10^3$; (e) $\delta = 9.5 \times 10^3$.

from the central region of flow. For $\delta = 3.5 \times 10^3$, in Fig. 5(b), two period-1 orbits distribute above and in the street, respectively. On the period-1 orbit above the street, the particles move from left to right. In Fig. 6, for the period-1 orbit, the maximal Lyapunov exponent is -0.254, so the orbit is stable. But, on the orbit in the street, the particles move in an opposite direction, i.e. from right

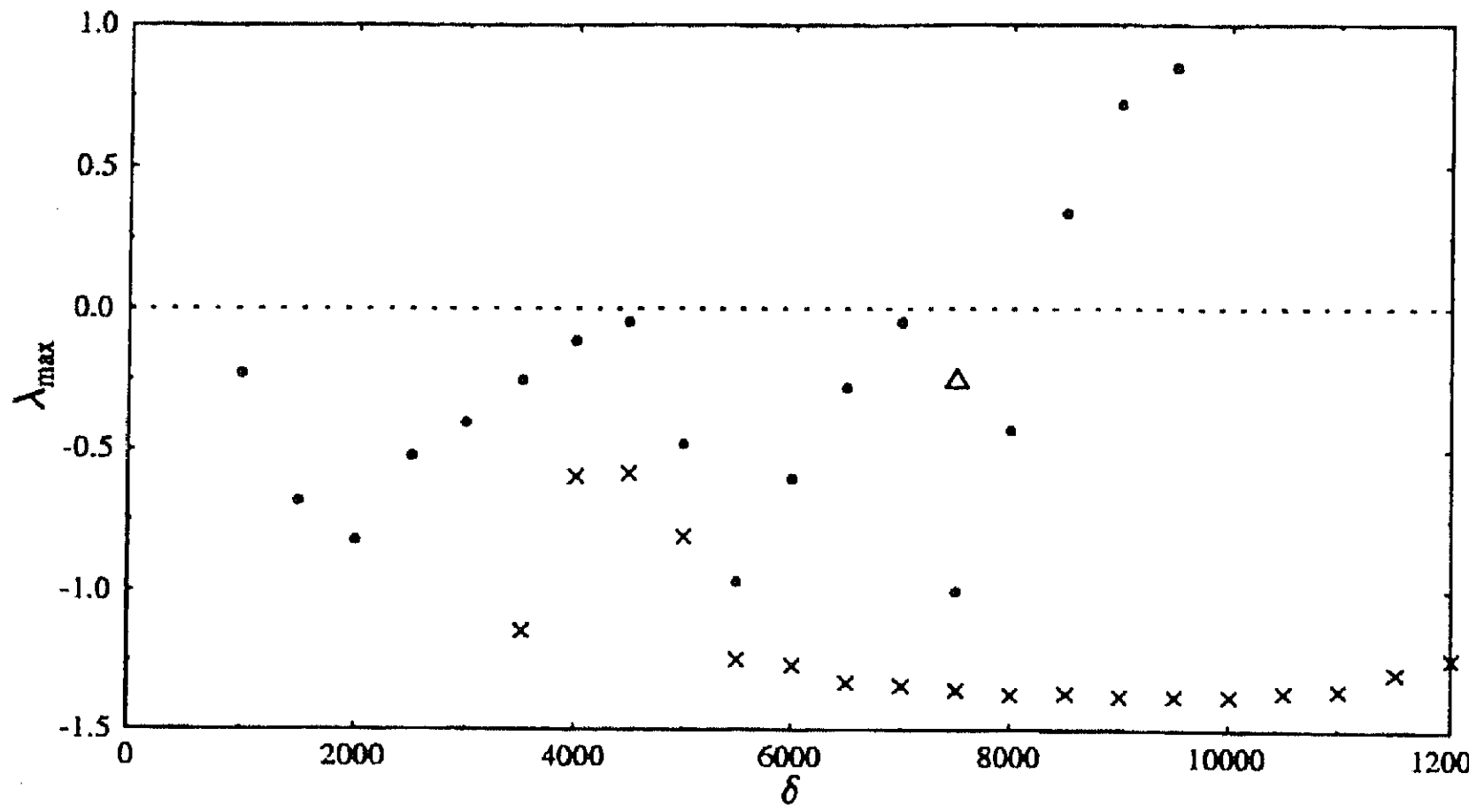

Fig. 6. Variation of the maximal Lyapunov exponent λ_{max} with δ. Besides the period-3 orbit for $\delta = 7.5 \times 10^3$ labeled by a triangle, the attractors above and in the street are marked by dots and crosses, respectively.

to left. The maximal Lyapunov exponent is -1.144, so the orbit is stable. For the two period-1 orbits, the corresponding basins of attraction are plotted in Fig. 7(b). One is similar to that in Fig. 7(a), the other is distributed in two local zones. The basin for the orbit in street is surrounded by that for the orbit above street. For $\delta = 6.0 \times 10^3$, a period-2 orbit above the street and a period-1 orbit in the street are drawn in Fig. 5(c). On the period-2 orbit above the street, the particles move from left to right. In Fig. 6, for the period-2 orbit, the maximal Lyapunov exponent is -0.604, so the orbit is stable. But, on the orbit in the street, the particles move in an opposite direction, i.e. from right to left. The maximal Lyapunov exponent is -1.268, so the orbit is stable. The corresponding basin of attraction is plotted in Fig. 7(c), which is similar to Fig. 7(b). For $\delta = 7.5 \times 10^3$, a combined period-4 orbit with a period-3 above the street and a period-1 orbit in the street are drawn in Fig. 5(d). On the period-4 and period-3 orbits above the street, the particles move from left to right. But, on the orbit in the street, the particles move in an opposite direction, i.e. from right to left. In Fig. 6, for the period-4, period-3 and period-1 orbits, the maximal Lyapunov exponent are -1.003, -0.245 and -1.356, respectively, so the orbits are stable. The corresponding basin of attraction is plotted in Fig. 7(d). The geometry of basin is different from the above ones in Figs. 7(a)–7(c). Some points near $y = 1$ escape from the basin of attraction in the dispersion of particles. For $\delta = 9.5 \times 10^3$, a quasi-periodic or chaotic orbit above the street and a period-1 orbit in the street are drawn in Fig. 5(e). On the orbit above the street, the particles move from left to right. In Fig. 6, for the orbit, the maximal Lyapunov exponent is 0.850, so the orbit is chaotic. But, on the orbit in the street, the particles move in an opposite direction, i.e. from right to left. The maximal Lyapunov exponent is -1.356, so the orbit is stable. The corresponding basin of attraction is plotted in Fig. 7(e). For the period-1 orbit in the street, the geometry of basin is similar to that in Fig. 7(d). But, for the chaotic orbit above the street, escaped points in Fig. 7(e) permeate into the basin of attraction in Fig. 7(d), so that the geometry of basin is fractal. From those examples, we can conclude that along with the increases of density ratio, initial points distributed in the central region of flow escape more and more. At the same time, the particle trajectories bifurcate from periodic orbits to chaotic orbits.

In order to explain the existence of attractors in the flow field, we take the period-1 and period-2 orbits for $\delta = 6.0 \times 10^3$ as an example. In Fig. 8, we present the values of V_x, V_y, u_y and $(Au_y - V_y)f_d - B$ along two orbits. For the period-2 orbit above the street, we plot it in two times of the streamwise

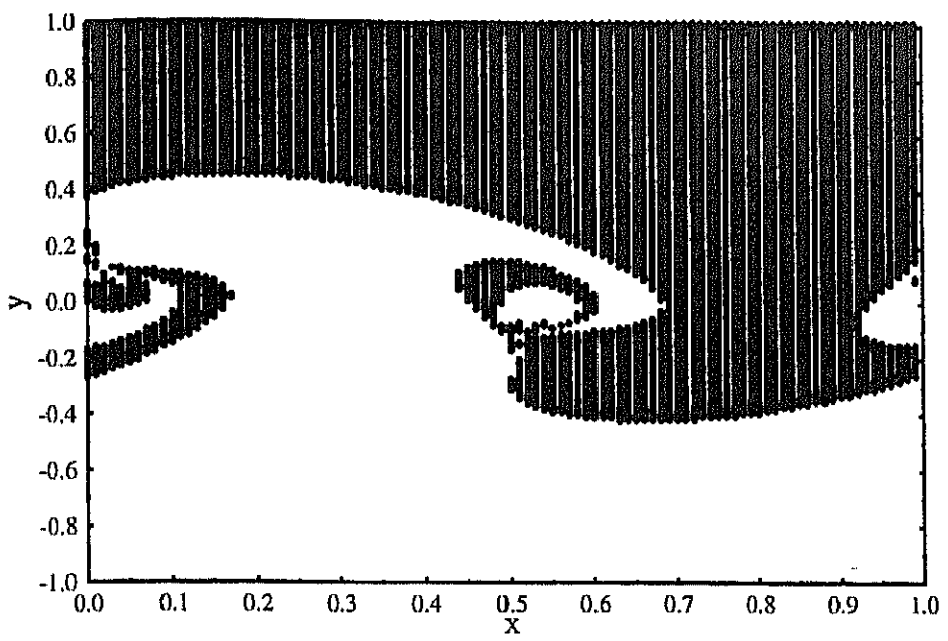

(a)

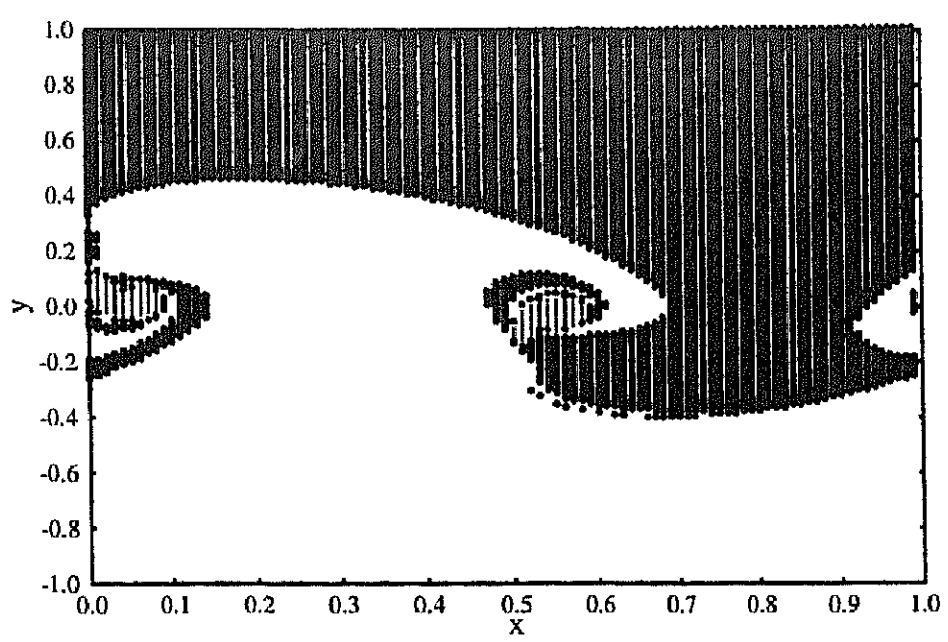

(b)

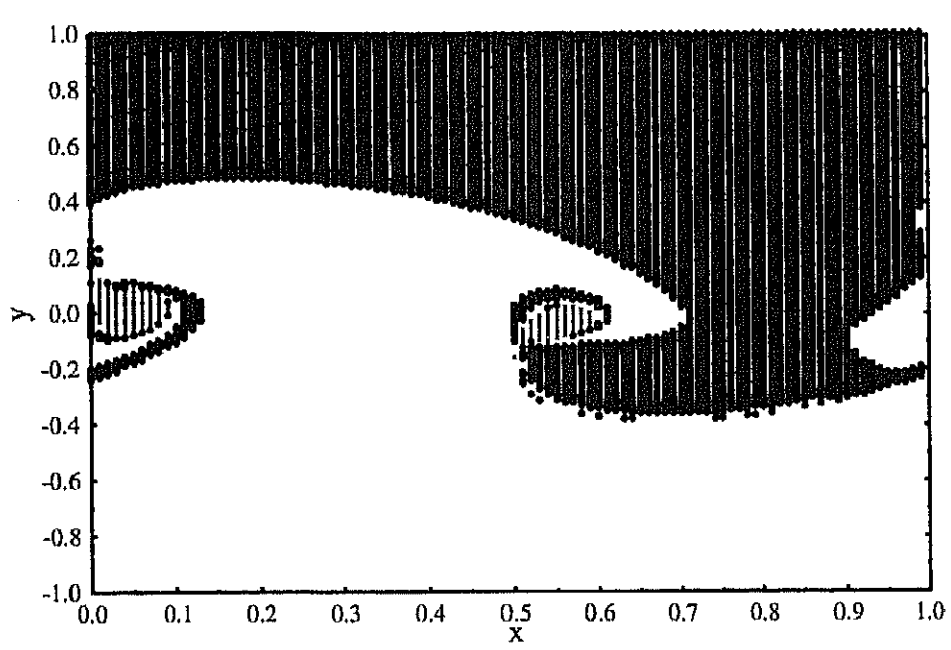

(c)

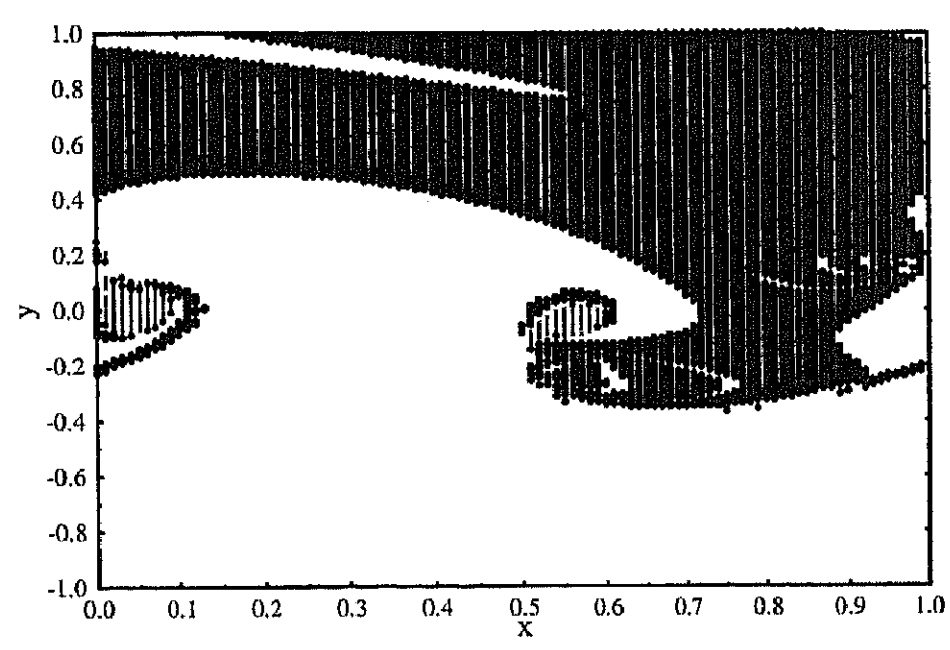

(d)

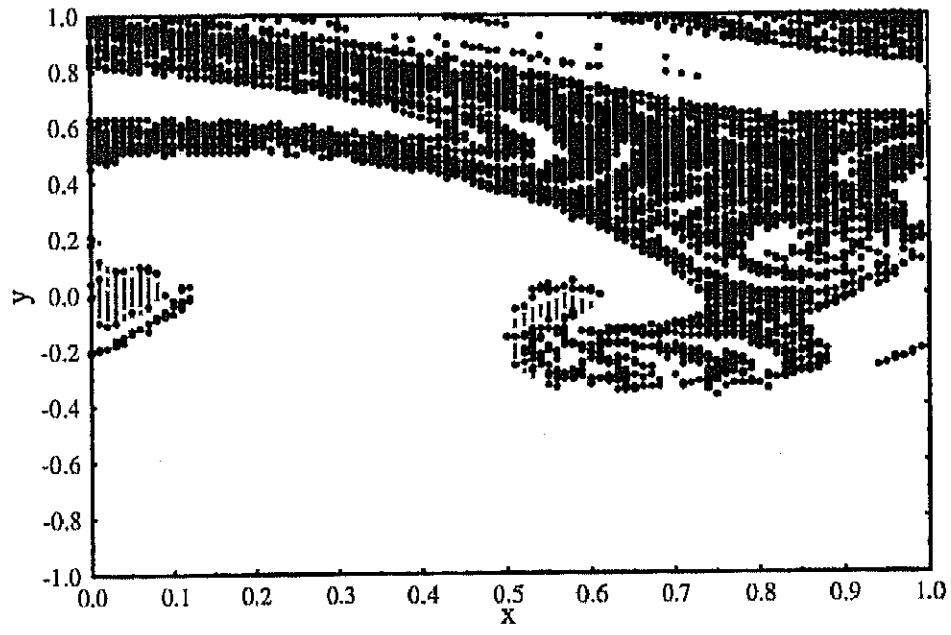

(e)

Fig. 7. Basins of attraction corresponding to the typical trajectories in Fig. 5 for (a) $\delta = 1.0 \times 10^3$; (b) $\delta = 3.5 \times 10^3$; (c) $\delta = 6.0 \times 10^3$; (d) $\delta = 7.5 \times 10^3$; (e) $\delta = 9.5 \times 10^3$. In Figs. 7(b)–7(e), besides two local zones marked by thinner lines for the basin of period-1 orbit in the street, the global zone presents the basin for attractors above the street.

periodic length in Fig. 8(a). Since $V_x > 0$ in $x \in [0, 2)$, the motional direction of particles is from left to right. (1) When a particle moves from $x = 0$ to $x = 0.486$, the negative term $(Au_y - V_y)f_d - B$ causes decrease of V_y from 0.050 to -0.285. At the same time, it leads to increase for the term $(Au_y - V_y)f_d - B$. (2) When the particle moves from $x = 0.486$ to $x = 0.930$, the positive term

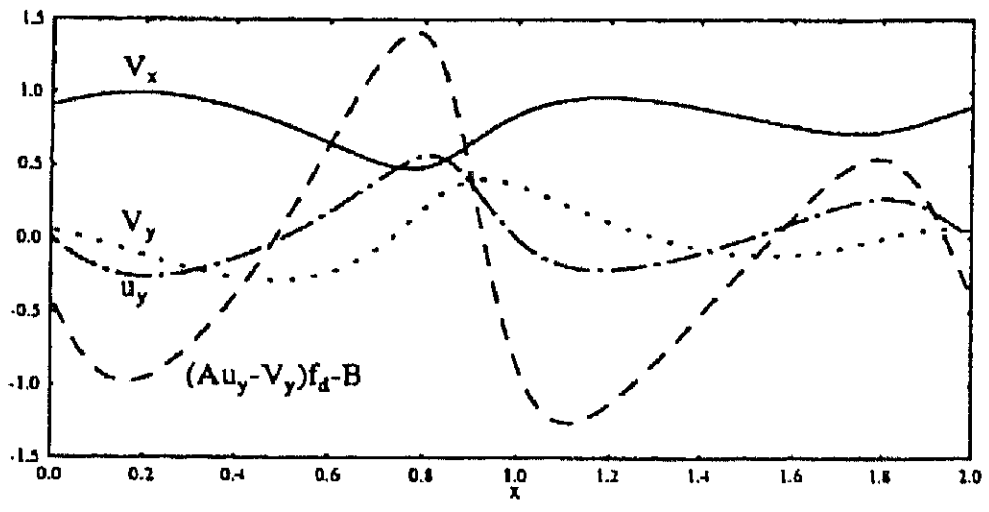

(a)

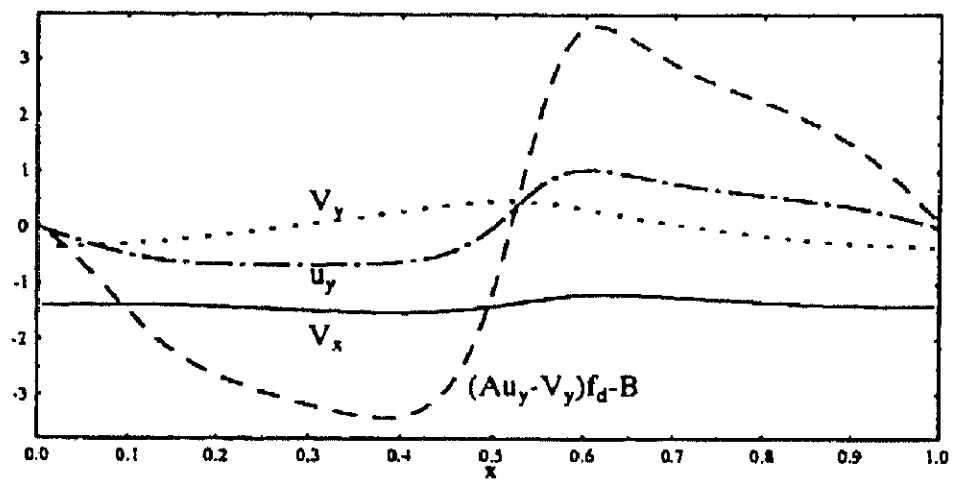

(b)

Fig. 8. Distribution of V_x, V_y, u_y and $(Au_y - V_y)f_d - B$ along x on (a) a period-2 orbit above the street; (b) a period-1 orbit in the street for $\delta = 6.0 \times 10^3$.

$(Au_y - V_y)f_d - B$ causes increase of V_y from -0.285 to 0.404. At the same time, it leads to decrease for the term $(Au_y - V_y)f_d - B$. (3) When the particle moves from $x = 0.930$ to $x = 1.554$, the negative term $(Au_y - V_y)f_d - B$ causes decrease of V_y from 0.404 to -0.115. At the same time, it leads to increase for the term $(Au_y - V_y)f_d - B$. (4) When the particle moves from $x = 1.554$ to $x = 1.946$, the positive term $(Au_y - V_y)f_d - B$ causes increase of V_y from -0.115 to 0.067. At the same time, it leads to decrease for the term $(Au_y - V_y)f_d - B$. (5) When the particle moves from $x = 1.946$ to $x = 2$, the negative term $(Au_y - V_y)f_d - B$ causes decrease of V_y from 0.067 to 0.050. At the same time, it leads to increase for the term $(Au_y - V_y)f_d - B$. According to the periodic boundary condition, when the particle reaches $x = 2$, it goes back to $x = 0$. Therefore, the combination of the drag term and gravity term in the vertical direction has a periodic vibration along with the variation of the vertical velocity of particles and makes the period-2 orbit. In Fig. 8(b), for the period-1 orbit in the street, we plot it in the streamwise periodic length. Since $V_x < 0$ in $x \in [0, 1)$, the motional direction of particles is from right to left. In a similar way to Fig. 8(a), the term $(Au_y - V_y)f_d - B$ brings into a periodic vibration of particles and makes the period-1 orbit. In [Burns *et al.*, 1999], by considering the drag term, the essential dynamics takes place on the two-dimensional centre manifolds. To compare with the result, we find the bifurcation process disappears when the gravity term in Eq. (8) is eliminated. From the above observation, we can conclude that the drag term and gravity term lead to the bifurcation behavior in dilute particle dispersion. The motional direction of particles and distribution of u_y determine the vertical position of attractors.

4. Effects of Spatial Parameters in Flow Field on Dilute Particle Dispersion

In Sec. 2, we show three types of streamline topology in the Kármán vortex street flow at different spatial parameters h. In Sec. 3, we present the dilute particle dynamics for the flow field with $h = 0.3$. In the following, we increase the spatial parameter h to consider its effects on dilute particle dispersion.

For $h = 0.410998$, along with the increase of density ratio, a bifurcation diagram y versus δ is drawn in Fig. 9. The global evolution is similar to that in Fig. 4. However, the bifurcation of period-1 attractor above the street is delayed. The period-1 orbit above the street bifurcates to a period-2 orbit at $\delta = 6.6 \times 10^3$. The period-2 orbit bifurcates to a period-4 orbit at $\delta = 1.04 \times 10^4$. In $\delta = 1.04 \times 10^4 - 1.2 \times 10^4$, the period-4 orbit bifurcates further to a quasi-periodic or chaotic orbit. A period-3 orbit above the street emerges at $\delta = 7.0 \times 10^3$ and bifurcates in $\delta = 7.0 \times 10^3 - 8.3 \times 10^3$. At $\delta = 8.3 \times 10^3$, a crises happens, so that the quasi-periodic or chaotic orbit above the street disappears. Moreover, the occurrence of period-1 attractor in the street is shifted earlier at $\delta = 2.0 \times 10^3$. A bifurcation of period-3 orbit in the street emerges in $\delta = 9.4 \times 10^3 - 1.1 \times 10^4$.

For $h = 0.6$, along with the increase of density ratio, a bifurcation diagram y versus δ is drawn in Fig. 10. The global evolution is similar to that in Fig. 9. However, the bifurcation of period-1 attractor above the street is delayed. The period-1 orbit above the street bifurcate to a period-2 orbit at $\delta = 9.1 \times 10^3$. The period-2 orbit is preserved in $\delta = 9.1 \times 10^3 - 1.2 \times 10^4$. At the same time, the occurrence of period-1 attractor in the street is shifted earlier at $\delta = 2.0 \times 10^2$. Moreover,

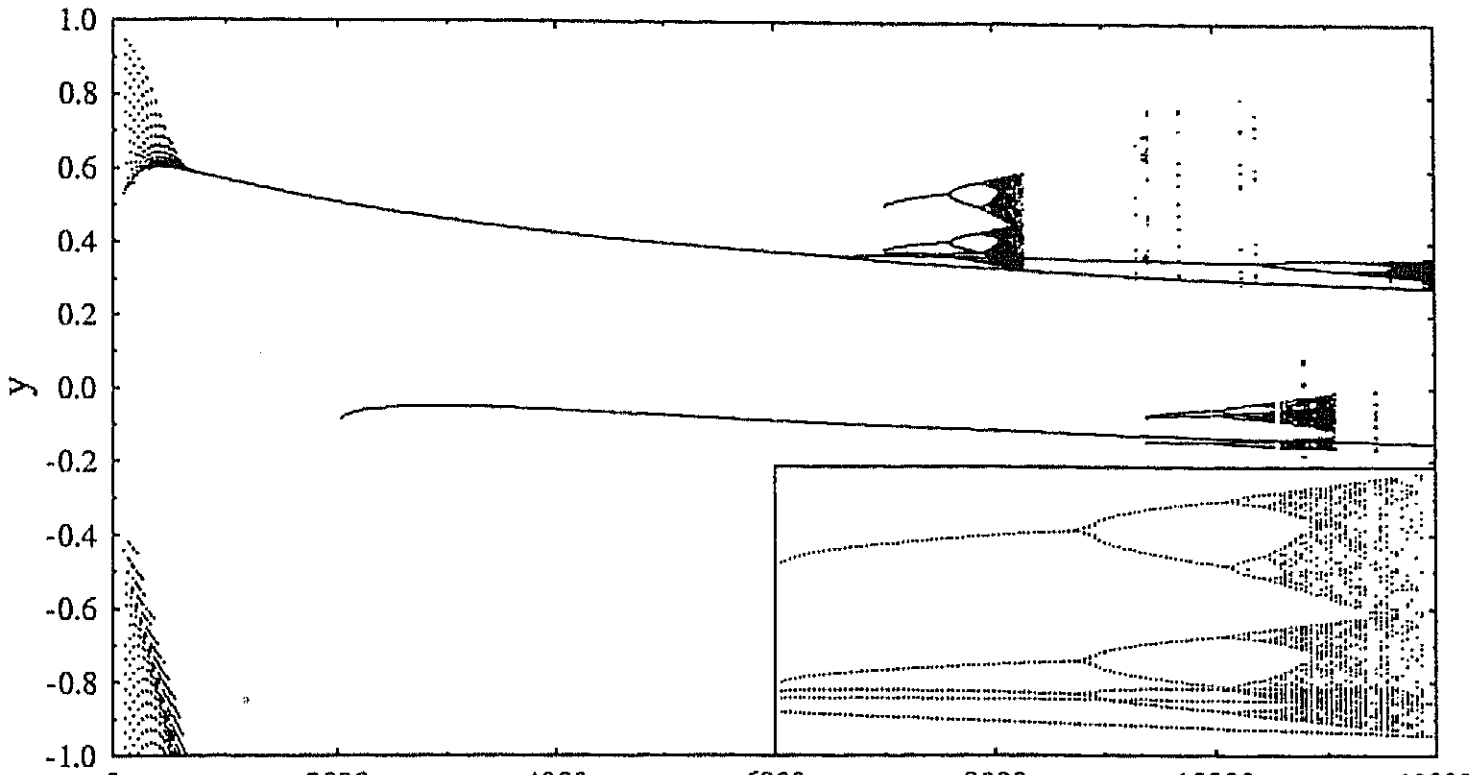

Fig. 9. A bifurcation diagram with $h = 0.410998$ for a continuous range of δ showing the vertical position of particles at $x = 0$. The dense bifurcation zone $\delta \in [7000, 8300]$ above the street is enlarged and redrawn in the bottom-right corner of the figure.

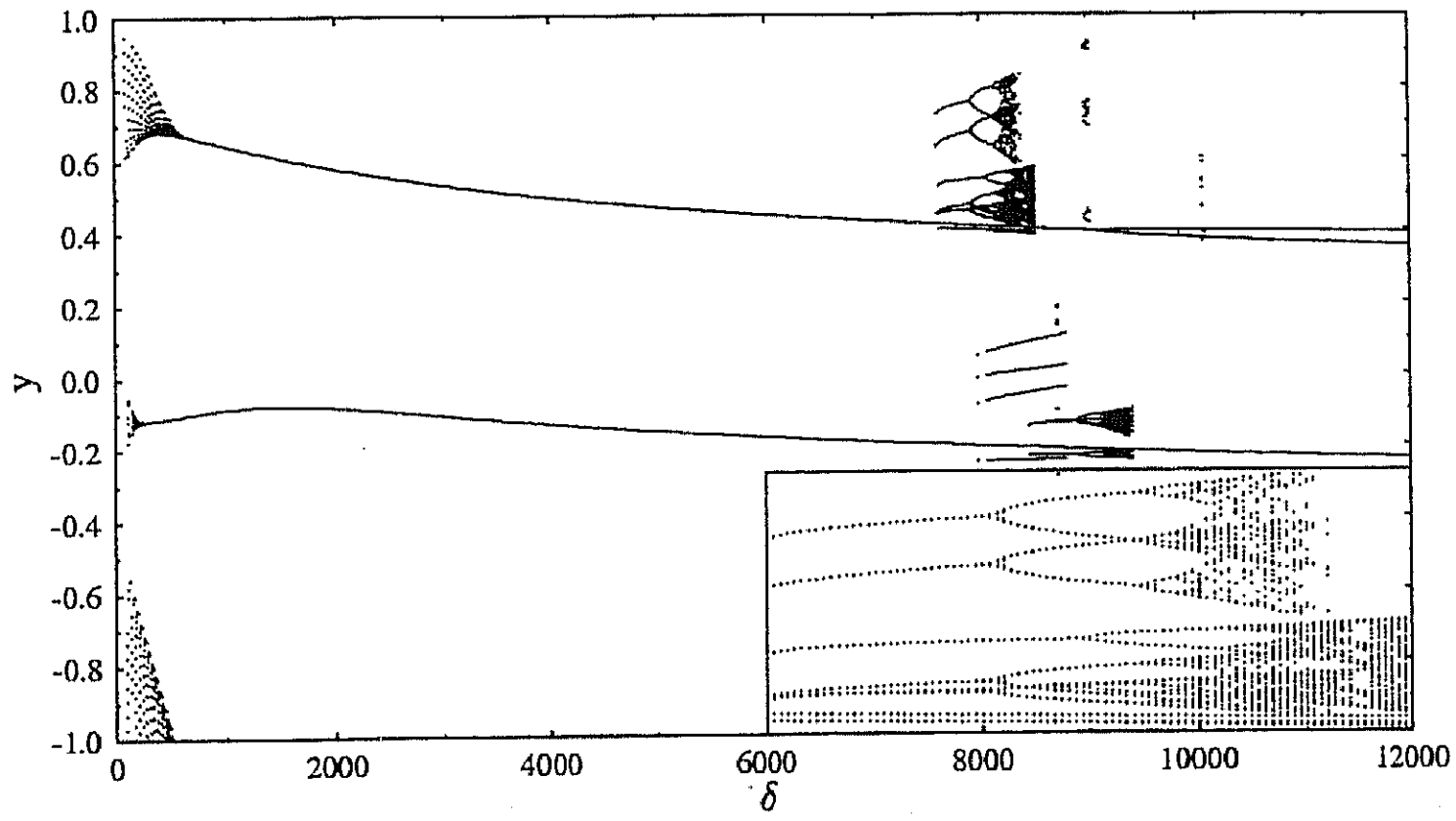

Fig. 10. A bifurcation diagram with $h = 0.6$ for a continuous range of δ showing the vertical position of particles at $x = 0$. The dense bifurcation zone $\delta \in [7600, 8500]$ above the street is enlarged and redrawn in the bottom-right corner of the figure.

at $\delta = 7.6 \times 10^3$, a period-4 and a period-3 orbit emerge above the street. They bifurcate further to two quasi-periodic or chaotic orbits and disappear at $\delta = 8.4 \times 10^3$ and $\delta = 8.5 \times 10^3$, respectively. In $\delta = 8.0 \times 10^3 - 9.4 \times 10^3$, a similar bifurcation process of more attractors emerges in the street. In $\delta = 8.0 \times 10^3 - 8.8 \times 10^3$, a period-4 orbit preserves in the street. In $\delta = 8.4 \times 10^3 - 9.4 \times 10^3$, a bifurcation of period-3 orbit exists in the street.

Thus, along with the increase of h, a period-1 orbit above the street bifurcates slower to a quasi-periodic or chaotic orbit, as well as a period-1 orbit in the street emerges earlier. Besides the main attractors in the flow field, more and more local attractors also appear above and in the street.

5. Conclusion

Under the variation of spatial parameters, we have shown three types of streamline topology in a Kármán vortex street flow. For the motion of dilute particles in the Kármán vortex street flow, there

exist a route of bifurcation to a chaotic orbit and more attractors in a bifurcation diagram for the proportion of particle density to fluid density. Along with the increase of spatial parameters in the flow field, the bifurcation process is suspended, as well as more and more attractors emerge. In the motion of dilute particles, a drag term and gravity term dominate and result in the bifurcation phenomenon.

Acknowledgment

This work was supported in part by the National Key Program for Developing Basic Science G1999032801-11.

References

Burns, T. J., Davis, R. W. & Moore, E. F. [1999] "A perturbation study of particle dynamics in a plane wake flow," *J. Fluid Mech.* **384**, 1–26.

Chung, J. N. & Troutt, T. R. [1988] "Simulation of particle dispersion in a axisymmetric jet," *J. Fluid Mech.* **186**, 199–222.

Clift, R., Grace, J. R. & Weber, M. E. [1978] *Bubbles, Drops and Particles* (Academic, NY).

Ganan-Calvo, A. M. & Lasheras, J. C. [1991] "The dynamics and mixing of small spherical particles in a plane, free shear layer," *Phys. Fluids* **A3**, 1207–1217.

Hussain, A. K. M. F. & Hayakawa, M. [1987] "Eduction of large-scale organized structures in a turbulent plane wake," *J. Fluid Mech.* **180**, 193–229.

Lorenz, E. N. [1963] "Deterministic nonperiodic flow," *J. Atoms. Sci.* **20**, 130–141.

Marcu, B. & Meiburg, E. [1996] "The effect of streamwise braid vortices on the particle dispersion in a plane mixing layer. I. Equilibrium and their stability," *Phys. Fluids* **A8**, 715–733.

Marcu, B., Meiburg, E. & Raju, N. [1996] "The effect of streamwise braid vortices on the particle dispersion in a plane mixing layer. II. Nonlinear particle dynamics," *Phys. Fluids* **A8**, 734–753.

Maxey, M. R. & Riley, J. J. [1983] "Equation of motion for a small rigid sphere in a nonuniform flow," *Phys. Fluids* **26**, 883–889.

Maxey, M. R. [1987] "The motion of spherical particles in a cellular flow field," *Phys. Fluids* **30**, 1915–1928.

Milne-Thomson, L. M. [1979] *Theoretical Hydrodynamics*, 5th edition (The Macmillan Press Ltd).

Okude, M. [1981] "Rearrangement of the Karman vortex street modes," *Trans. Jpn. Soc. Aero. Space Sci.* **24**, 95–105.

Okude, M. & Matsui, T. [1987] "Correspondence of velocity fluctuations to flow patterns in a Karman vortex street at low Reynolds numbers," *Trans. Jpn. Soc. Aero. Space Sci.* **30**, 80–90.

Panton, R. L. [1984] *Incompressible Flow* (John Wiley).

Press, W. H., Teukolsky, S. A., Vetterling, W. T. & Flannery, B. P. [1992] *Numerical Recipes in C*, 2nd edition (Cambridge University Press.)

Rubin, J., Jones, C. K. R. T. & Maxey, M. [1995] "Setting and asymptotic motion of aerosol particles in a cellular flow field," *J. Nonlin. Sci.* **5**, 337–358.

Shimada, I. & Nagashima, T. [1979] "A numerical approach to ergodic problem of dissipative dynamical system," *Prog. Theor. Phys.* **61**, 1605–1616.

Tang, L., Wen, F., Yang, Y., Crowe, C. T., Chung, J. N. & Troutt, T. R. [1992] "Self-organizing particle dispersion mechanism in a plane wake," *Phys. Fluids* **A4**, 2244–2251.

Tio, K.-K., Ganan-Calvo, A. M. & Lasheras, J. C. [1993] "The dynamics of small, heavy rigid spherical particles in a periodic Stuart vortex flow," *Phys. Fluids* **A5**, 1679–1693.

Willimson, C. H. K. [1998] "The existence of two stages in the transition to three-dimensional of a cylinder wake," *Phys. Fluids* **31**, 3165–3168.

Wolf, A., Swift, J. B., Swinney, H. L. & Vastano, J. A. [1985] "Determining Lyapunov exponents from a time series," *Physica* **D16**, 285–317.

Wu, Z.-B. & Ling, G.-C. [1994] "Theoretical study on topological structure of Kármán vortex street flow field," *Acta Aerodyn. Sin.* **12**, 355–362 (in Chinese).